Saturating Intrinsic Detection Efficiency of Superconducting Nanowire Single-Photon Detectors via Defect Engineering

Weijun Zhang,[1,2,3,*] Qi Jia,[1,3] Lixing You,[1,2,3,4,†] Xin Ou,[1,3,4,‡] Hao Huang,[1,3] Lu Zhang,[1,2] Hao Li,[1,2,3] Zhen Wang,[1,2,3] and Xiaoming Xie[1,2,3]

[1] *State Key Lab of Functional Materials for Informatics, Shanghai Institute of Microsystem and Information Technology (SIMIT), Chinese Academy of Sciences (CAS), 865 Changning Rd., Shanghai 200050, China*

[2] *Center for Excellence in Superconducting Electronics (CENSE), Chinese Academy of Sciences (CAS), 865 Changning Rd., Shanghai 200050, China*

[3] *University of Chinese Academy of Sciences, 19 A Yuquan Rd, Shijingshan District, Beijing 100049, China*

[4] *Center of Materials Science and Optoelectronics Engineering, University of Chinese Academy of Sciences, Beijing 100049, China*

(Received 25 April 2019; revised manuscript received 24 August 2019; published 17 October 2019)

A superconducting nanowire single-photon detector (SNSPD) has played a significant role in numerous applications for visible and near-infrared photon detection. SNSPDs with high system detection efficiency (SDE greater than 90%) would enable remarkable experiments in quantum information processing. Currently, niobium nitride- (NbN) based SNSPDs are widely used in practical applications since they can operate in an inexpensive compact closed-cycle cryostat. However, it is a challenge to realize a NbN SNSPD with saturated intrinsic detection efficiency (IDE) while maintaining its high SDE at near-infrared wavelengths. We develop a postprocessing method to enhance the IDE of NbN SNSPDs to saturation without sacrificing SDE through defect engineering by a 20-keV helium ion irradiation. The enhancement of IDE is achieved because of the irradiation-induced reduction of the superconducting energy gap and the electron density of states at the Fermi level as determined by the electrical transport measurements. The change in the optical absorptance of the irradiated SNSPD is insignificant at the resonant wavelength as confirmed by the measured optical reflectance and SDE. By taking advantage of the IDE enhancement, the SDE of an irradiated device is significantly increased from 49% to 92% at 2.2 K for a 1550-nm wavelength.

DOI: 10.1103/PhysRevApplied.12.044040

I. INTRODUCTION

Controllable modification of the physical properties of thin films is crucial for their application in functional devices. Ion implantation or irradiation is regarded as a powerful tool for this purpose. Ion implantation technology has been widely used in the microelectronic industry for impurity doping of semiconductor materials and devices. Meanwhile, defect engineering by ion irradiation has been demonstrated to be an effective approach for adjusting the physical, chemical, or electrical properties of semiconductors [1–4].

For years, studies on the ion irradiation effects in superconductors have elicited remarkable interest from both science and application perspectives because of the controlled impurity or lattice disorder induced to the superconductors through ion irradiation that would aid in understanding superconductivity [5,6] and adjusting the performance of superconducting devices [7]. The ion irradiation effects depend on the mass and energy of the irradiating ions, as well as the type of superconductors used. For example, in the case of high-critical temperature (T_c) oxide superconductors, heavy ion irradiations can generate columnar or cluster defects, which act as vortex pinning centers and may enhance the irreversible field and superconducting critical current density [8,9].

Niobium nitride (NbN) has been extensively explored because of its attractive physical properties for plasmonic nanostructures [10] and has been widely used to fabricate superconducting devices, such as superconducting nanowire single-photon detectors (SNSPDs) [11]. Previously, a study reported that NbN showed a robust resistance to irradiation damage (e.g., fast neutron irradiation [12]) in comparison with other superconductors. Its result was attributed to the highly defective nature of NbN. The effects of ion irradiation (200-keV Ar) damage on both single crystal and polycrystalline NbN films have also been investigated [6], where a reduction in the electron

*zhangweijun@mail.sim.ac.cn
†lxyou@mail.sim.ac.cn
‡ouxin@mail.sim.ac.cn

density of states at the Fermi level (N_0) was inferred to the vacancies generated through ion irradiation.

SNSPDs have demonstrated unparalleled performance in near-infrared photon detection with high system detection efficiency (SDE greater than 90%) [13,14], low dark count rate (DCR less than 1 cps) [15], high count rate (CR greater than 1.5 Gcps) [16], and high temporal resolution (<15 ps) [17,18]. These detectors are successfully employed in quantum information processing [19], high-speed optical communication [20], and time-of-flight ranging systems [21,22]. Recently, significant loop-hole-free Bell tests [23,24] were performed using high efficiency detectors to close the detection loophole. The rapid development in molecular science [25] and space observatories [26] also provides a unique opportunity and challenge for the ultrasensitivity and high-efficiency SNSPDs for near- to midinfrared single-photon detection.

The operating principle of the SNSPD can be simplified as follows [11,27]. An incident photon can break up hundreds of Cooper pairs in the superconducting nanowire to form a hotspot or normal region. The growth of the normal region produces a transient resistance state, resulting in a voltage pulse in the read-out circuit, representing a detection event. The Joule heat is transferred to the substrate and then the nanowire returns to the superconducting state waiting for the subsequent photon. Intrinsic detection efficiency (IDE) or spectral sensitivity depicts the probability of a pulse generation in the nanowire when a photon is absorbed. The photon detection relies on the energy conversion of the absorbed photon into elementary excitations and hotspot generation in the superconducting nanowire, however, this process has remained unclear until today [28–30]. Additionally, in realizing a SNSPD with SDE near unity, all the factors that affect the SDE (i.e., IDE, AE, and OCE) must be optimized simultaneously [13,14,31], where AE is the optical absorption efficiency and OCE is the optical coupling efficiency.

Generally, IDE can be improved by fabricating devices with thin [32] or narrow [33] nanowires. It can also be enhanced by using a low superconducting energy gap (Δ) or low N_0 materials, such as WSi [13], MoSi [34], TaN [35], and MoN [30]. Notably, amorphous WSi SNSPDs (T_c, approximately 4 K) show well-pronounced saturated plateaus in SDE at bias current below the switching current when they detect the near-infrared photons. The saturated plateaus in SDE are empirically determined as the IDE reaches unity. The success of WSi SNSPDs has also elicited increasing interest for investigating the basic detection mechanism based on this material [36,37]. However, such WSi detectors are limited to the large kinetic inductance and require lower operating temperatures (<1 K).

For practical applications, SNSPDs are often fabricated using 5−8-nm-thick NbN or $Nb_1Ti_{1-x}N$ films, thereby forming 50−100-nm-wide nanowires. The NbN-based SNSPD operates at a temperature range of 2−4 K with a commercial Gifford-McMahon (GM) cryocooler. However, it remains challenging to achieve a saturated IDE for the near-infrared photons [14,31,38] because of the relatively high T_c (8−10 K) of the NbN films. Furthermore, both the thickness and width of the nanowire influence Δ as well as the AE [14,31]. Hence, simultaneously optimizing these parameters is technically challenging, which is crucial for achieving SDE close to unity. Therefore, a method to decouple the IDE and AE of SNSPDs (i.e., without modifying the geometric parameters and sacrificing AE) would be very useful to the design and fabrication of SNSPDs. Previous attempts have been made to enhance the IDE performance of SNSPDs by using various NbN chemical components [39], hybrid NbN/WSi structures [38], or bias-sputtered NbN films [40]. However, few reports on the postprocessing that can directly control and compare the performance of SNSPDs are available. The continuous modification on the detector performance may also provide interesting information for studying the photon detection mechanism.

Herein, we report an alternative method to tune the physical properties of superconducting NbN ultrathin films and SNSPDs by using the He ion irradiation. We investigate the modification of the polycrystalline NbN films based on different He ion fluences ranging from 1×10^{14} to 5×10^{16} ion cm^{-2} at an ion energy of 20 keV. Both Δ and N_0 are continuously decreased by the ion irradiation, and the AE of the irradiated film remains essentially constant at the resonant wavelength of 1550 nm. Then the SNSPDs are irradiated by He ions and their IDE is significantly improved. The SDE of an SNSPD is increased from 49% to 92% at 2.2 K and more than 90% at 2.5 K for 1550 nm. Furthermore, the long-term stability (>1.5 years) of the irradiated devices is characterized. The irradiation effects on the detector's performances (e.g., timing jitter, count rate, and dark count rate) are also discussed.

II. METHODS

Polycrystalline NbN film is deposited on a distributed Bragg reflector (DBR) substrate through direct current reactive magnetron sputtering in a mixed Ar and N_2 atmosphere at room temperature, with the thickness controlled by the deposition time. A DBR made of fifteen SiO_2/Ta_2O_5 bilayers is used for enhancing the AE of the nanowires to near unity [14]. For the electrical transport measurements, a four-point probing microbridge (40-μm long, 60-μm wide) is patterned using ultraviolet lithography and etched by reactive ion etching (RIE). To measure the optical reflectance as a function of wavelength, a spectrophotometer (PerkinElmer, Lambda950) is used with a scanning step of 1 nm and a relative uncertainty of less than 0.2%.

Three SNSPDs (called $d1$, $d2$, and $d3$) with the typical meander geometry are selected for this experiment. The devices are fabricated from NbN thin films on DBR substrates through electron beam lithography and RIE, as shown in Fig. 1(a). These devices are fabricated in the same batch. To guarantee a reliable optical coupling, their active areas are designed to be 18×18 μm^2. Figure 1(b) shows a scanning electron microscope (SEM) image of the nanowire used in this study, whose nominal width and spacing are both 80 nm.

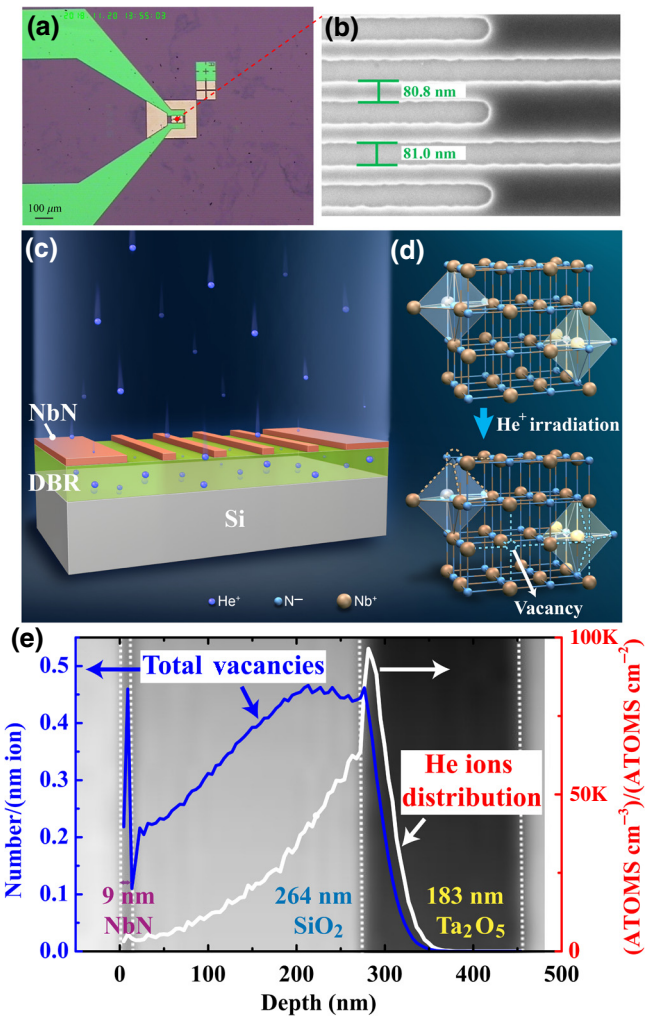

FIG. 1. (a) Enlarged optical photo of a SNSPD chip. The purple regions are covered with NbN film while the green regions are the DBR substrate. Golden marks are used for optical alignments. The active area is indicated with a red dot in the front of the dashed line. (b) SEM image of a nanowire with an 80-nm width and 160-nm pitch. (c) Schematic of the He ion irradiation process on SNSPD (not to scale). (d) Possible NbN crystal structures before (top panel) and after (bottom panel) He ion irradiation. In the bottom panel, dashed circles indicate the possible vacancies created by irradiation. (e) Simulated vacancy and ion distributions as a function of depth by using the SRIM method. The background is embedded with a TEM photo of a 9-nm-thick NbN film on the DBR substrate (only the first SiO_2/Ta_2O_5 bilayer is shown).

In this study, a low-energy He ion irradiation with an ion energy of 20 keV is produced by a 300-mm medium-current ion implanter (Nissin, Exceed 2300RD) at room temperature. The choice of the He ion aims to prevent chemical reactions and an ion etching effect. The irradiation fluence (F_i) ranges from 1×10^{14} to 5×10^{16} ion cm^{-2}. Figure 1(c) shows the schematic of the ion irradiation process on the SNSPD, where the ejected ions fully cover the entire chip. Figure 1(d) shows a possible change in the NbN crystal structure before and after the He ion irradiation. In the ion irradiation process, the ejected He ions can knock the Nb or N ions far from their regular sites and then create vacancies, indicated with dashed circles in the bottom of Fig. 1(d). Figure 1(e) illustrates the depth distributions of He ions and irradiation-induced vacancies, simulated for a 9-nm-thick NbN film on a $SiO_2/Ta_2O_5/Si$ substrate. The simulation is conducted using the Monte-Carlo method with the computer code of the stopping and range of ions in matter (SRIM) [41]. The result indicates that the project range of He ions is located at the SiO_2/Ta_2O_5 interface. In other words, the top NbN layer is modified by the vacancies rather than He ions.

To further exclude the possibility of the ion etching effect in our experiment, the thickness of the NbN film is analyzed by using a transmission electron microscope (TEM, FEI Talos F200). For example, two neighboring thin-film samples (with a size of 5×5 mm^2) are diced from one 2-in. wafer. The measured thicknesses of the unirradiated and irradiated (at the highest $F_i = 5 \times 10^{16}$ ion cm^{-2}) films are 10.6 ± 0.3 nm and 10.8 ± 0.2 nm, respectively. Thus, the thickness modification induced by ion irradiation is insignificant. The uncertainty in this measurement is dominated by the thickness variation (less than 3.5%) of the whole wafer and the accuracy (approximately 0.1 nm) of the TEM measurement.

To characterize the optical–electrical properties of the SNSPD, the device is packaged with a lens single-mode fiber and then cooled in a 2.2-K GM cryostat, as reported previously [14]. In the SDE measurements (see the setup in Appendix A), a high-precision optical power meter (Keysight Inc., 81624B) is used to calibrate the input power as well as the attenuation of the attenuators. During the measurement, a MEMS optical switch (Thorlabs Inc., OSW12-1310E, split ratio of approximately 1) and the power meter are used to monitor the input power. The optical power is first attenuated to −48.92 dBm, then further attenuated to −108.92 dBm by using two cascaded attenuators with a calibrated attenuation of −60 dB. The final input optical power corresponds to a photon flux of approximately 1×10^5 photon s^{-1}, with a laser repetition rate of approximately 20 MHz and a typical laser pulse width of approximately 0.1 ps (Calmar FPL1550). This ensures an averaged photon number of approximately

0.005 photon per pulse. SDE is determined by the expression SDE equals (CR-DCR)/IPR [13], where CR is the response pulse count rate and DCR is the dark count rate, which is the average of the CR collected for 10 s when the light is blocked by the shutter, and IPR is the input photon rate. To improve the CR performance of our detector, a regular surface-mount resistor is connected in series to the SNSPD chip in the package block [42,43]. The SDE at 1550 nm measured in this work, with a relative uncertainty of approximately 3% [14], refers to the photons polarized parallel to the nanowire. The measurements of electrical transport properties are performed using a Quantum Design PPMS-9 system with a temperature stability of ±3 mK. The magnetic field is perpendicular to the sample substrate. During the measurements, the samples undergoes zero-field cooling to remove the magnetic flux trapping effect and are successively cooled to 2 K. Then, the resistivity (ρ) of the samples is recorded as a function of the rising temperature. T_c is determined from the temperature at which $\rho(T)$ drops to 50% of its normal state value at 20 K (ρ_{20K}).

III. RESULTS AND DISCUSSION

A. Transport properties of irradiated NbN films

Figure 2 shows the fluence dependence of T_c (left axis) and ρ_{20K} (right axis) for NbN films with different thicknesses (5, 7, 9, and 11 nm) in a linear scale. In the right axis, only the ρ_{20K} of the 7-nm-thick NbN sample is shown because the typical thickness used in our detector fabrication is around 7 nm. For the unirradiated thin films (i.e., $F_i = 0$), T_c is thickness dependent, which varies from 9.58 K (at 11 nm) to 5.47 K (at 5 nm). For each thickness, both T_c and ρ_{20K} vary continuously with an increase of He ion fluences. By using the 7-nm-thick film as an example, at the highest $F_i = 5 \times 10^{16}$ ion cm^{-2}, the ratio of T_c and ρ_{20K} is approximately 0.82 and 1.90, respectively, compared to their initial values. By increasing the fluence further, we speculate that the reduction of T_c would reach a saturation because of the saturation of the vacancy density [5].

Figure 3 shows the resistivity as a function of temperature for the 7-nm-thick NbN films irradiated at various He ion fluences. As the fluence increases, the normal state resistivity continuously increases. The inset of Fig. 3 shows the superconducting transition regime for the same curves in an enlarged scale. The resistivity is normalized by its own ρ_{20K} value. The superconducting transition width (ΔT_c) is determined by the temperature width at which the normalized ρ/ρ_{20K} drops from 0.9 to 0.1. It is found that the ΔT_c values of the films irradiated at various fluences are all in a range of 1.50–1.55 K (for more details, see Table I). This small variation (approximately 0.05 K) in ΔT_c indicates that ion irradiation at the present fluences causes no damage to the ultrathin film sufficient to impair its uniformity. Therefore, the use of ion irradiation can be a promising tool to tune the physical properties of thin films without degrading their quality.

To evaluate the material parameters, the resistivity as a function of temperature is recorded at different magnetic fields up to 9 T. Figure 4(a) shows the comparison of the $\rho(T)$ curves of the 7-nm-thick NbN films irradiated at $F_i = 0$ and 1×10^{16} ion cm^{-2}. ΔT_c of the $\rho(T)$ curves becomes larger in the magnetic field. For instance, at a magnetic field of 5 T, ΔT_c is about 2.70 K ($F_i = 0$) and 3.20 K ($F_i = 1 \times 10^{16}$ ion cm^{-2}), respectively, compared

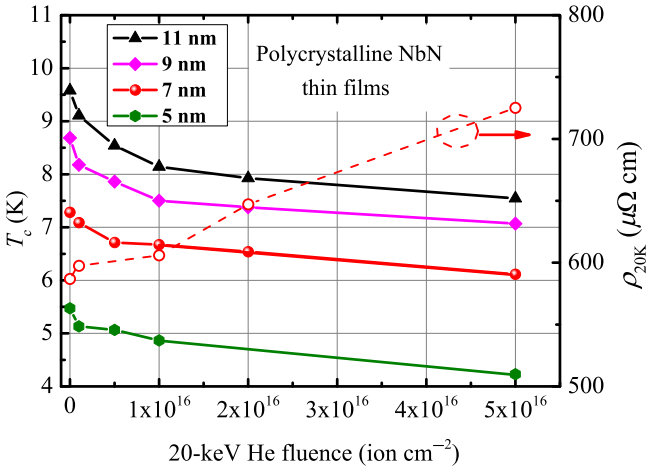

FIG. 2. Left axis: Fluence dependence of the superconducting critical temperature (T_c, solid scatters) for NbN films with varying thicknesses. Right axis: Fluence dependence of the resistivity measured at 20 K (ρ_{20K}, open circles) for the 7-nm-thick NbN film.

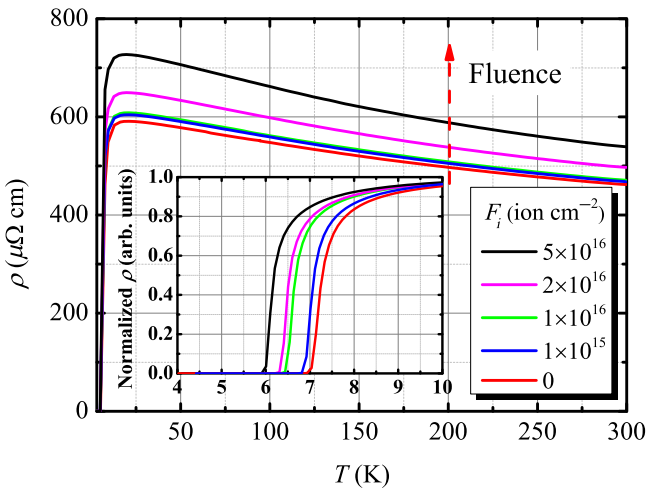

FIG. 3. Temperature dependence of resistivity for a 7-nm-thick NbN film at various irradiated fluences. Inset: normalized resistivity as a function of temperature in an enlarged scale.

TABLE I. Material parameters of the 7-nm-thick NbN thin films on DBR substrates and the SNSPD *d*3 irradiated at different fluences (F_is).

	F_i (ion cm^{-2})	ρ ($\mu\Omega$ cm)			$T_c(0)$ (K)	$\Delta T_c(0)$ (K)	$\xi_{GL}(0)$ (nm)	D (cm^2 s^{-1})	$\Delta(0)$ (meV)	N_0 (nm^{-3} eV^{-1})
		300 K	20 K	*RRR*						
7 nm NbN film	0	462	587	0.787	7.28	1.55	5.1	0.44	1.11	24.4
	1×10^{15}	468	597	0.784	7.09	1.55	5.2	0.45	1.08	23.4
	1×10^{16}	471	606	0.777	6.67	1.50	5.6	0.47	1.01	21.7
	2×10^{16}	497	647	0.768	6.54	1.52	5.7	0.49	0.99	19.7
	5×10^{16}	539	725	0.743	6.11	1.53	5.9	0.50	0.93	17.1
8 nm NbN SNSPD *d*3	0	297	360	0.825	8.64	1.53	4.2	0.35	1.31	50.2
	1×10^{16}	382	482	0.793	7.16	1.53	4.8	0.37	1.09	34.8

to the values (approximately 1.5 K) at the zero field. The broadening of ΔT_c with increasing F_i in a magnetic field can be evidence of increasing lattice disorder, since the electronic density correlation function at finite wave numbers is very sensitive to scattering based on the Bardeen-Cooper-Schrieffer (BCS) theory [44]. For each given magnetic field, T_c at an upper critical magnetic field (B_{c2}) is determined to be the temperature when the resistivity drops to 50% of its normal state value. Thus, in turn, B_{c2} as a function of temperature (i.e., T_c) is obtained from the abovementioned measurements, and the data are plotted in Fig. 4(b). Dashed lines are the linear fits to the measured data. The material parameters, for example, N_0, electron diffusion coefficient (D), and Ginzburg–Landau (G–L) coherence length (ξ_{GL}) [45] are deduced by using the dirty-limit relation [46] as follows

$$B_{c2}(0) = 0.69 T_c \frac{dB_{c2}}{dT}|_{T=T_c}, \tag{1}$$

$$\xi_{GL} = \sqrt{\frac{\Phi_0}{2\pi B_{c2}(0)}}, \tag{2}$$

$$N_0 = B_{c2}(0)\left(0.69 T_c \frac{4ek_B}{\pi}\rho_n\right)^{-1}, \tag{3}$$

$$D = \frac{4k_B}{\pi e}\left(\frac{dB_{c2}}{dT}|_{T=T_c}\right)^{-1}. \tag{4}$$

Here, e is the electron charge, k_B is the Boltzmann constant, and Φ_0 is the flux quantum. The energy gap at $T=0$, $\Delta(0)$, which decreases with increasing F_i, can be calculated using the BCS relation [35] as follows:

$$\Delta(0) = 1.76 k_B T_c. \tag{5}$$

Note that the ratio of $\Delta(0)/k_B T_c \sim 1.7-2.1$ is not constant and changes with resistivity. This ratio often depends on the quality of the NbN thin film [47,48]. However, the selected value does not affect our results in any manner because we are interested in the relative changes of $\Delta(0)$. Based on the previous study [35], the value of 1.76 is used here.

Table I shows the deduced material parameters of 7-nm-thick NbN films irradiated at various fluences. These parameters are notably influenced by the fluences. For example, as F_i increases from 0 to 5×10^{16} ion cm^{-2}, ξ_{GL} and D increase by 16% and 14%, respectively, while $\Delta(0)$ and N_0 decrease by 16% and 30%, respectively. In addition, ρ, T_c, and ΔT_c are also displayed in this table. It is found that the listed residual resistivity ratio

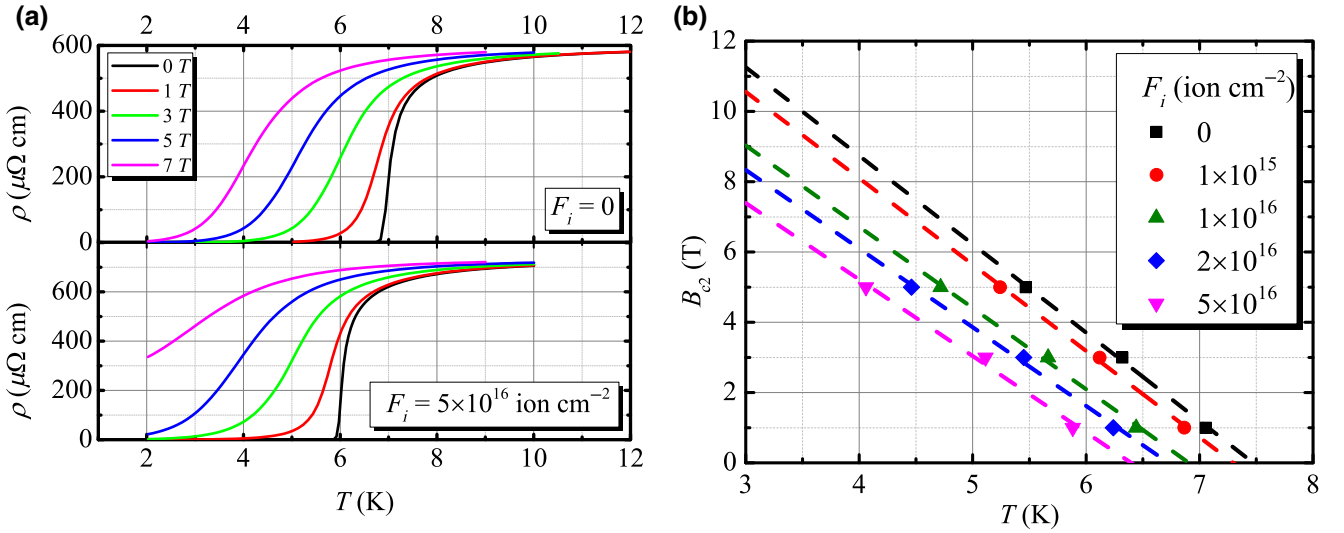

FIG. 4. (a) Temperature dependence of the resistivity for 7-nm-thick NbN films irradiated with $F_i = 0$ and 1×10^{16} ion cm^{-2}, recorded at different magnetic fields as indicated by the labels. (b) Temperature dependence of the upper critical field (B_{c2}) for the 7-nm-thick NbN film at different fluences. The experimental data and fitting results are indicated by solid scatters and dashed lines, respectively.

(RRR)($= \rho_{300K}/\rho_{20K}$) continuously decreases with F_i from 0.787 to 0.743. Such a reduction was also observed for NbN films with reduced thickness [32], however, the causes are different in the two cases. In our case, it may be attributed to the increasing disorders induced by ion irradiation.

B. Optical properties of irradiated NbN films

Characterizing the optical properties of the irradiated thin films is important because of their applicability as optical detectors. Figure 5(a) shows the measured reflectance (r) as a function of wavelength (λ) for the 7-nm NbN film at various F_is. The variation of r caused by different fluences at the resonant wavelength ($\lambda = 1550$ nm) is less than 1%.

As Fig. 5(b) shows, the $r(\lambda)$ curves have a slight redshift (approximately 22 nm) from 1567 nm ($F_i = 0$) to 1589 nm ($F_i = 5 \times 10^{16}$ ion cm^{-2}) using the wavelength position of the minimum reflectance (r_{min}) as a reference. Here, r_{min} is the minimum of each $r(\lambda)$ curve shown in Fig. 5(a), irradiated at different fluences. Meanwhile, r_{min} varies from 0%

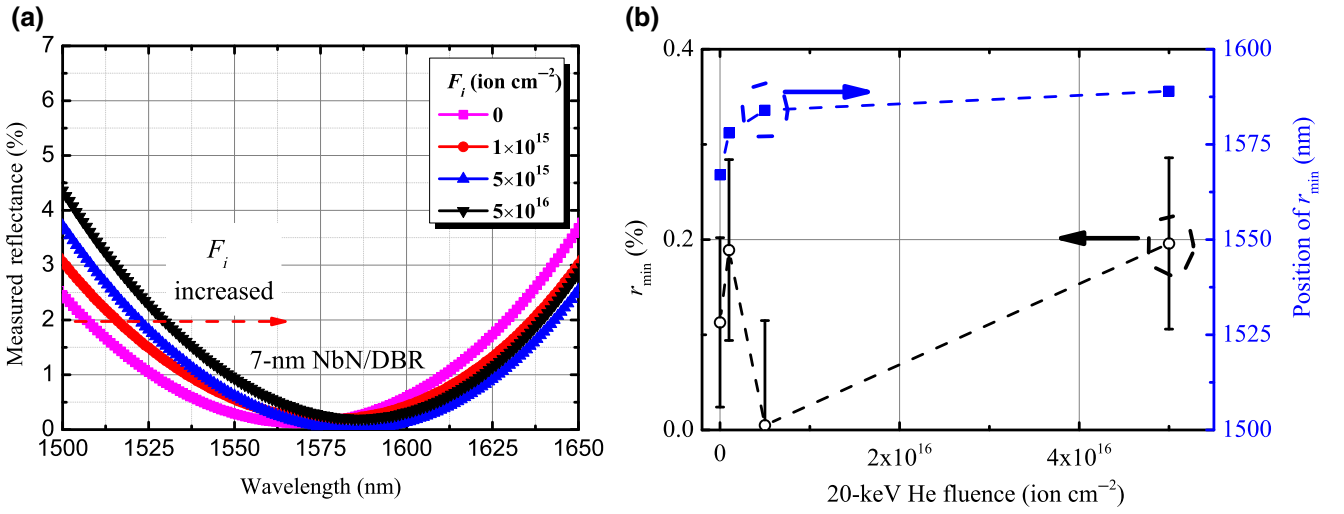

FIG. 5. (a) Measured wavelength dependence of the reflectance (r) for the 7-nm-thick NbN film on the DBR substrate, irradiated at different fluences. (b) Fluence dependence of minimum reflectance (r_{min}) and its wavelength position (solid squares). As fluence increases, r_{min} slightly redshifts.

to 0.3%. At $F_i = 5 \times 10^{16}$ ion cm^{-2}, $r_{\min} \sim 0.2\%$. For NbN films on the DBR substrate

$$AE_f = 1 - r - TR \approx 1 - r, \tag{6}$$

where AE_f is the absorptance of the film and $TR \sim 0$ is the transmittance of the DBR at its resonant band [14]. Due to the broad band (approximately 200 nm) and low reflectance features (absorbed by NbN film) of the optical design, the ion irradiation has a negligible effect on the optical absorptance of NbN thin films at its resonant band for SNSPD applications.

To further reveal the He ion irradiation effects on the optical properties of the materials, a commercial ellipsometer (J. A. Woollam Co. Inc., RC2) is used to measure their optical parameters, such as refractive index (n) and extinction coefficient (k). Since the thickness of the NbN thin film is much smaller than that of the SiO_2 layer of the DBR substrate, a 268-nm-thick SiO_2 single layer on a Si wafer is adopted to simulate the irradiation effects on the top SiO_2 layer. The He ion irradiation is performed with a fluence of approximately 5×10^{16} ion cm^{-2} at a 20-keV He ion energy. The optical parameters of the SiO_2 layer are measured before and after irradiation, respectively. As shown in Appendix D, the effects of irradiation on the SiO_2 layer result in an increase (<2%) in the measured n [49,50]. As revealed by the numerical simulation, the increased n of the top SiO_2 layer shows a wavelength shift effect (approximately 5 nm) on the optical absorptance of the NbN nanowire on a DBR cavity. However, the changes on the absorption of the NbN nanowire are quite small and negligible.

Furthermore, the irradiation effects on the optical parameters of the NbN nanowire are also investigated by experiment and simulation (see Appendix D). In the simulation, using the measured optical parameters of the unirradiated and/or irradiated NbN thin films and the SiO_2 layer, the peak of the NbN nanowire's absorptance shows a redshift from 1535 to 1563 nm, with a slight decrease (approximately 0.6%) in the peak value. This result may qualitatively explain the wavelength redshift effect in the reflectance measurement of the irradiated NbN thin films shown in Fig. 5. This means that the irradiation-induced changes of the optical parameters of NbN may lead to the changes of absorptance (reflectance). However, due to the presence of the DBR cavity, the effects caused by the changes of the optical parameters of NbN are weakened, especially at the resonant wavelength of 1550 nm. For example, the variations of the nanowire's absorptance near the resonant wavelengths (e.g., 1550 ± 40 nm) are less than 2% (see Appendix D), which is smaller than our SDE measurement accuracy. Thus, the irradiation effects on the optical absorptance of a NbN nanowire on the DBR cavity are insignificant at the resonant wavelength.

C. He ion irradiation effects in SNSPDs

The irradiation effects in SNSPDs are investigated with a 20-keV He ion irradiation. Table II provides detailed information of the SNSPDs used in the experiment. The detectors (i.e., $d1$, $d2$, and $d3$) are irradiated at F_i of 1×10^{15}, 5×10^{15}, and 1×10^{16} ion cm^{-2}, respectively. The parameters of SNSPDs, such as T_c, switching current (I_{sw}), and SDE, are recorded both before and after irradiation. I_{sw} is defined as the highest I_b that a device can sustain before it switches to the normal state. It is found that the irradiation degrades T_c and I_{sw}, while the SDE is improved for all the detectors measured, especially for devices $d2$ and $d3$.

Figure 6 shows SDE as a function of the bias current (I_b) for SNSPD before and after irradiation. The maximum SDE (SDE_{max}) significantly increases for the irradiated devices. A weak saturated plateau emerges for the SNSPDs irradiated at F_i of 5×10^{15} and 1×10^{16} ion cm^{-2}, indicating the enhancement of their IDEs. An empirical sigmoid function fitting [31] is applied to the experimental data, which are shown with dashed lines in the figure. The asymptotic values (SDE_{asy}) of the fittings imply the hypothetical maximum SDEs for IDEs of 100%. As mentioned, the SDE of SNSPD can be expressed as SDE equals IDE times OCE times AE [13]. In the asymptotic condition, assuming IDE as unity and the change in AE induced by irradiation as negligible, SDE depends mainly on OCE. For example, the SDE_{asy} values for device $d3$ before and after irradiation are almost the same, indicating that OCE does not significantly change and suggesting a good optical

TABLE II. Comparison of the SNSPD parameters before and after 20-keV He ion irradiation. Here d, w, and p denote the thickness, width, and pitch of the nanowire, respectively.

	Device $d1$		Device $d2$		Device $d3$	
d (nm)	7.5		8		8	
w/p (nm)	80/160		80/140		80/140	
F_i (ion cm^{-2})	0	1×10^{15}	0	5×10^{15}	0	1×10^{16}
T_c (K)	8.3	8.1	8.6	7.5	8.6	7.2
ρ_{20K} ($\mu\Omega$ cm)	394	435	377	463	360	482
I_{sw} (μA) @2.2 K	16.8	16.7	19.4	13.5	18.9	9.3
SDE_{max}@2.2 K	84%	88%	49%	92%	57%	81%

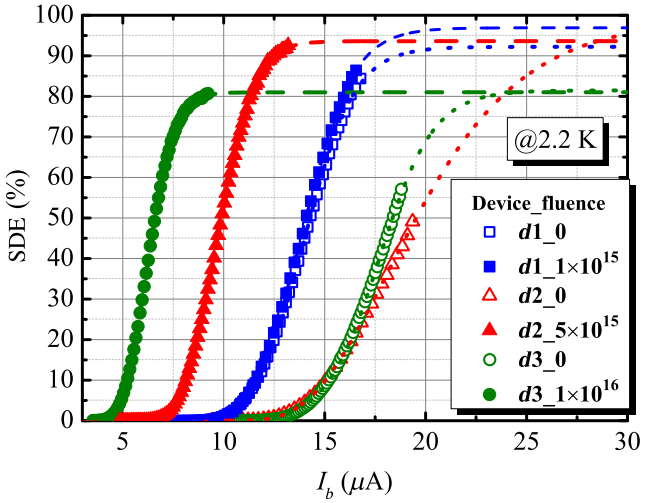

FIG. 6. SDEs as a function of I_b for the SNSPDs before (open scatters) and after (solid scatters) He ion irradiation. The dotted and dashed lines are the sigmoid function fittings for the experimental data before and after irradiation, respectively.

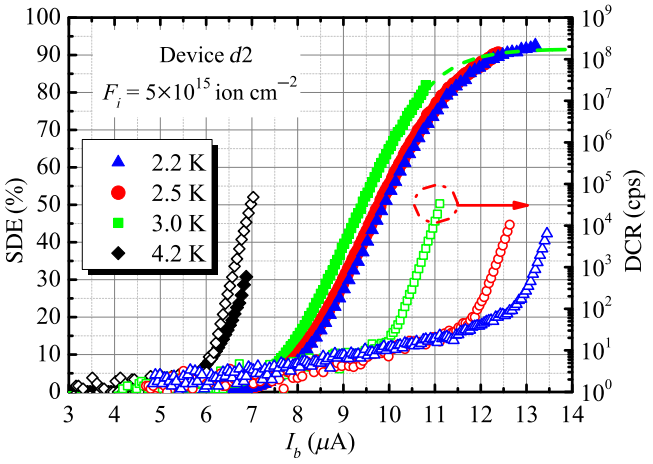

FIG. 7. SDEs (solid scatters) and DCRs (open scatters) of device $d2$ as a function of I_b, measured at different temperatures for the device $d2$ irradiated at $F_i = 5 \times 10^{15}$ ion cm^{-2}. The green dashed line is the sigmoid function fitting.

coupling. However, due to the limitation in the accuracy of the optical coupling, a slight difference (<5%) remains in the SDE_{asy} values for two subsequent measurements of devices $d1$ and $d2$. Nevertheless, the results indicate that no significant change is observed in AE of the nanowire after the irradiation. Thus, the SDE enhancement is due mainly to the improvement of IDE. Since the IDE is influenced by thickness, width, and constriction in the nanowire, directly comparing the IDE of the two different devices is difficult. Moreover, the maximum SDE of approximately 81% for device $d3$ is limited by the contamination on its surface, as found using an optical microscope.

Interestingly, the SDE of device $d2$ at $F_i = 5 \times 10^{15}$ ion cm^{-2} is significantly enhanced from 49% to 92% at 2.2 K. Its SDE is shown in Fig. 7 as a function of I_b at various temperatures. With the increasing temperature, the saturated platform gradually degrades. However, an SDE of 90.4% is obtained at 2.5 K. Unlike the previous results achieved at 2.1 K, the operating temperature has been further improved. Even at 3 K, the SDE still exceeds 80%, rendering the device attractive for a compact refrigerator compatible with space applications [51].

The temperature dependence of B_{c2} is also measured for the devices irradiated at $F_i = 0$ and 1×10^{16} ion cm^{-2} (not shown). The material parameters of device $d3$ are calculated from the experimental data, as shown in Table I (lower panel). ΔT_c remains nearly unchanged, consistent with the results of the NbN films. $\Delta(0)$ and N_0 of the irradiated samples are expected to decrease and D remains almost constant compared with the original values. N_0 is larger in the nanowire than in the thin film because a little thicker layer is used for SNSPD. The reduction ratio of N_0 between unirradiated and irradiated detectors is approximately 1.44, slightly smaller than the value (approximately 2.0) reduction in I_{sw}.

Finally, the long-term stability of the irradiated device is investigated as shown in Fig. 8, given that it is significant for its practical implementation. Note that our devices are placed in a drying cabinet at room temperature after performing the experiments. We recharacterize the superconducting properties and SDE of the same irradiated device $d3$ more than 1.5 years after it was first measured. The results show a slight increase in resistivity (approximately 1.07×) and slight reduction in I_{sw} (approximately 0.97×). The SDEs in the two measurements are nearly the same, with values of 81% and 80%, respectively. The reduction in T_c is approximately 0.03 K. The normalized resistivity (ρ/ρ_{20K}) as a function of temperature for the two cases is shown in the inset of Fig. 8(a). Such an aging effect is also observed in unirradiated devices, excluding the irradiation influence. The reason for the aging effect may be attributed to the oxidation of the NbN thin film. Even with the slight aging effect, the saturated plateau on SDE is still well preserved and will not influence the use of the device.

D. Discussion and outlook

The reduction in $\Delta(0)$ as well as N_0 and increase in ρ_n are observed in our experiments with He ion irradiations. The mechanism may be explained by the increasing disorder in the NbN crystal lattice, caused by the irradiation-induced vacancies [5,6], which would decrease the electronics properties of the material. Furthermore, the ultrathin polycrystalline NbN films in this study demonstrate a stronger reduction (up to 23% for 5 nm) in T_c than that of thicker polycrystalline films (6%–7%, 45–135-nm

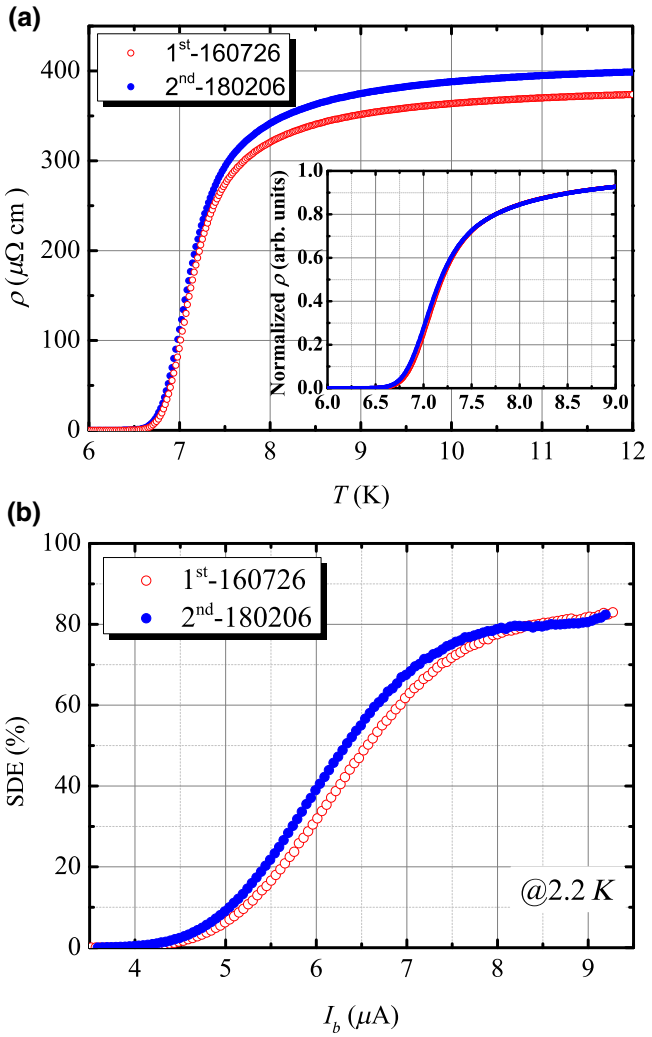

FIG. 8. Physical properties of the same irradiated device *d*3 measured at different periods, that is, first time (1st, open scatters) and >1.5 years after (2nd, solid scatters). (a) Temperature dependence of resistivity (inset, temperature dependence of the normalized resistivity in an enlarged scale). (b) Bias current dependence of SDE.

thick) irradiated with 200 keV Ar ions [6]. This phenomenon indicates that thinner films are more easily influenced by irradiation. Therefore, by combining the effects of the He ion irradiation and film thickness variation, a larger tunable range of T_c (9.6–4.8 K, in this study) is obtained, thereby providing a possible space for the investigation of the physical properties of NbN thin films.

Regarding the devices, a direct method to evaluate the influence of He ion irradiation on SNSPDs is introduced. The reasons why the irradiation does not induce significant geometrical constrictions to the nanowire may be explained by two main factors: first, the He ion irradiation is a nonetching process, preventing direct etching damage; second, irradiation-induced vacancies are normally point defects and the size is generally much smaller than the dimensions of the nanowire. The spatial distribution of the vacancies in the nanowire is nearly uniform.

To qualitatively understand the IDE enhancement caused by the changes of the material parameters, we utilize a simplified hotspot model [27], which describes the SNSPD response by an analytical expression. In this model, a superconducting nanostrip carries I_b, and a minimum energy $E_{\min}$ (or maximum wavelength) detectable by the nanostrip can be determined using the following equation:

$$E_{\min} = h\nu = \frac{hc}{\lambda} \geq \frac{N_0 \Delta^2 wd}{\zeta} \sqrt{\pi D \tau_{\text{th}}} \left(1 - \frac{I_b}{I_{\text{CD}}}\right), \tag{7}$$

where c is the speed of light, wd is the cross-section area of the nanowire, τ_{th} is the time scale of the quasiparticle multiplication process, and I_{CD} is the depairing critical current. As expressed in Eq. (7), if considering the irradiation-induced reduction of $\Delta(0)$ and N_0 as well the change of D, then the estimated $E_{\min}$ irradiated at $F_i = 1 \times 10^{16}$ ion cm^{-2} is reduced to nearly 50% of its unirradiated value. The reduced $E_{\min}$ implies an enhanced spectral sensitivity (i.e., IDE). In a word, the reduction of $\Delta(0)$ and N_0 greatly stimulates the generation and growth of the normal region after photon absorption, resulting in an improved photon response probability.

Note that Eq. (7) is derived in a model with several simplifications and holds certain limitations. Some disagreements on experimental results are found, for example, regarding the temperature dependence of D and Δ [28]. Recent studies [29,52] revealed that the photon detection process can be more complex, involving numerical simulations. Therefore, the mechanism is not reducible to a single equation. Further theoretical works are required to quantitatively understand the irradiation-induced IDE enhancement.

The method based on ion irradiation has several advantages. First, it is a postprocessing technology compatible with the microelectronics industry. Second, it aids in constructing a film with low T_c while retaining its uniformity. Third, it can relax the fabrication precision on the film thickness as well as the width of the nanowire and also extend the spectral responsivity of the device to the midinfrared or even far-infrared range by reducing $\Delta(0)$, similar to other WSi devices [25]. In the future, a few interesting works can be explored. First, to reveal the underlying mechanisms of the irradiated samples, an x-ray diffraction analysis on the NbN single crystal before and after He ion irradiation should be conducted. Second, investigations on the yield improvement by using either preirradiated NbN/DBR wafers or postirradiated SNSPDs would be interesting in the applications requiring large amounts of SNSPDs [53].

One of the prices of the irradiated device is the reduction of the switching current, which would increase the timing jitter (TJ) of the device. For example, TJ increases to 71 ps by a factor of approximately 1.7 after irradiation at a fluence of 5×10^{16} ion cm^{-2} (see Appendix B), which is mainly attributed to the reduced signal-to-noise ratio (SNR) of the output pulse, similar to the previous TJs of SNSPDs without irradiation [54]. The increase in TJ can be compensated with using a cryogenic amplifier since the SNR can be effectively improved [18]. In addition, due to the increase of the kinetic inductance (the normal state resistance) after irradiation, the normalized maximal photon-response count rate (PCR, i.e., CR-DCR) is reduced (e.g., with a reduction factor of approximately 1.4 at a fluence of 5×10^{16} ion cm^{-2}, see Appendix B). However, by having a proper resistor (R_s) in series with the device, the normalized maximal PCR before and after irradiation can be improved to 55 and 48 Mcps at a photon flux of 1×10^9 photon s^{-1}, with a reduction ratio of 1.1 (approximately equal to 55/48) (see Appendix B). To address the problems, a parallel nanowire configuration [55] may be used to improve the detection speed as well as the timing jitter.

The effect on DCR by the He ion irradiation is also interesting. As shown in Appendix C, we defined an onset normalized I_b at which the intrinsic DCR (iDCR) starts to be larger than 0.1 cps. It was found that, the onset normalized I_b after irradiation shifts to a lower value than the one before irradiation when both iDCRs were measured at the same operating temperature. The reason can be attributed to the reduced T_c by ion irradiation. However, at the same normalized temperature (T/T_c), iDCR has the nearly same current dependence. In practical applications, the detector often operates at a low bias current region (generally, $\leq 0.96 I_{sw}$), where the background DCR (bDCR) is dominant. The bDCR is proportional to the photon number of thermal radiation and/or stray light as well as IDE. Without considering the improvement on IDE, the direct influence of irradiation on DCR can be practically neglected.

IV. CONCLUSIONS

In summary, we report an alternative method to tune the physical properties of superconducting polycrystalline NbN ultrathin films and SNSPDs via defect engineering with He ion irradiation. The irradiation-induced vacancies in NbN films lead to a continuous decrease in the superconducting energy gap and the electron density of states at the Fermi level as the He ion fluence increases. The influence on the optical absorptance of the irradiated NbN film and/or nanowire on a DBR cavity at the resonant wavelength can be neglected, as revealed by the experiment and numerical simulation. By directly using the He irradiation on the SNSPDs, IDE and SDE are significantly improved. The SDE of an irradiated device at a He fluence of 5×10^{15} ion cm^{-2} is significantly enhanced from 49% to 92% at 2.2 K and more than 90% at 2.5 K for a 1550-nm wavelength. The irradiated devices demonstrate a good long-term stability over 1.5 years. The He ion irradiation is a useful tool for the SNSPD fabrication and development, such as relaxing the process requirements for the film thickness and linewidth control, IDE enhancement for longer wavelengths, and yield improvement. Moreover, the He ion irradiation may also be applied in the fabrication of other superconducting devices.

ACKNOWLEDGMENTS

We thank Tiangui You for helpful discussions. This work is supported by the National Key R&D Program of China (Grant No. 2017YFA0304000), the Science and Technology Commission of Shanghai Municipality under Grants No. 16JC1400402 and No. 18511110202, and the National Natural Science Foundation of China (NSFC Grants No. 61971409, No. 11622545, No. U1732268, No. 61874128, and No. 61851406).

APPENDIX A: EXPERIMENTAL SETUP FOR THE SNSPD CHARACTERIZATION

Figure 9 shows a schematic of the experimental setup used in our SDE measurement. Light emitted from a fiber-coupled laser is transmitted to three variable fiber attenuators followed by a MEMS optical switch, fiber polarization controller, and SNSPD under test. An antireflection coating (ARC) fiber is connected to a high precision optical power meter (Keysight Inc., 81624B, power range: -90 to $+10$ dBm). The split ratio of the optical switch is carefully calibrated by splicing the same ARC fiber to each branch of the switch. After calibration, the fiber connected to the SNSPD is spliced to the one of the switch branches. During the measurement, by switching the optical switch, the input light power to the SNSPD at a high light level can be monitored. A regular surface-mount resistor (R_s) is connected in series to the SNSPD chip in the package block.

APPENDIX B: TIMING JITTER AND COUNT RATE OF A SNSPD BEFORE AND AFTER IRRADIATION

We did the ion irradiation experiments on a different device $d4$ (with the same geometrical structure of the nanowire), but at a higher fluence of 5×10^{16} ion cm^{-2} than those (1×10^{16} ion cm^{-2}) presented in the main text.

Figure 10(a) shows SDE vs I_b for the device $d4$ before and after irradiation, measured at a low photon flux of 1×10^5 photon s^{-1}. The maximum SDE before and after irradiation are about 85% and 70%, respectively.

Figure 10(b) shows a comparison of TJ before and after irradiation. Before irradiation, the smallest TJ of the device $d4$ is about 41.4 ± 0.5 ps at 21.5 μA and increases

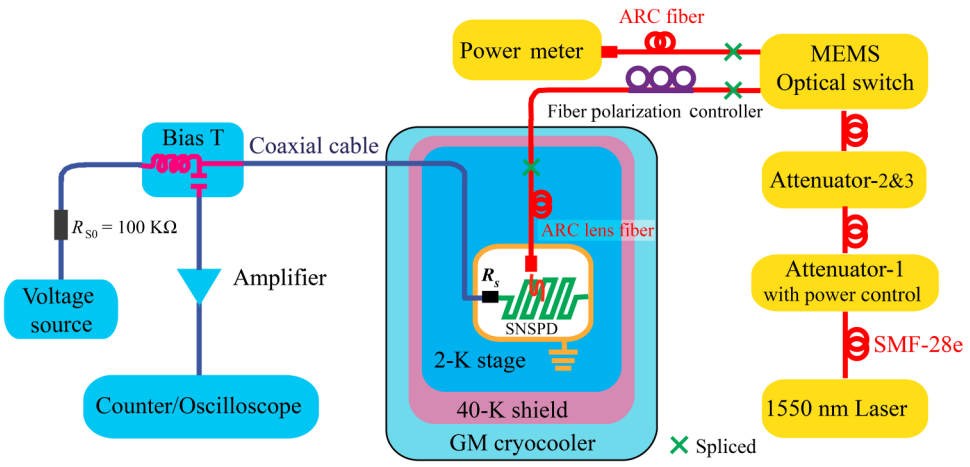

FIG. 9. Schematic of the experimental setup used for the SNSPD characterization.

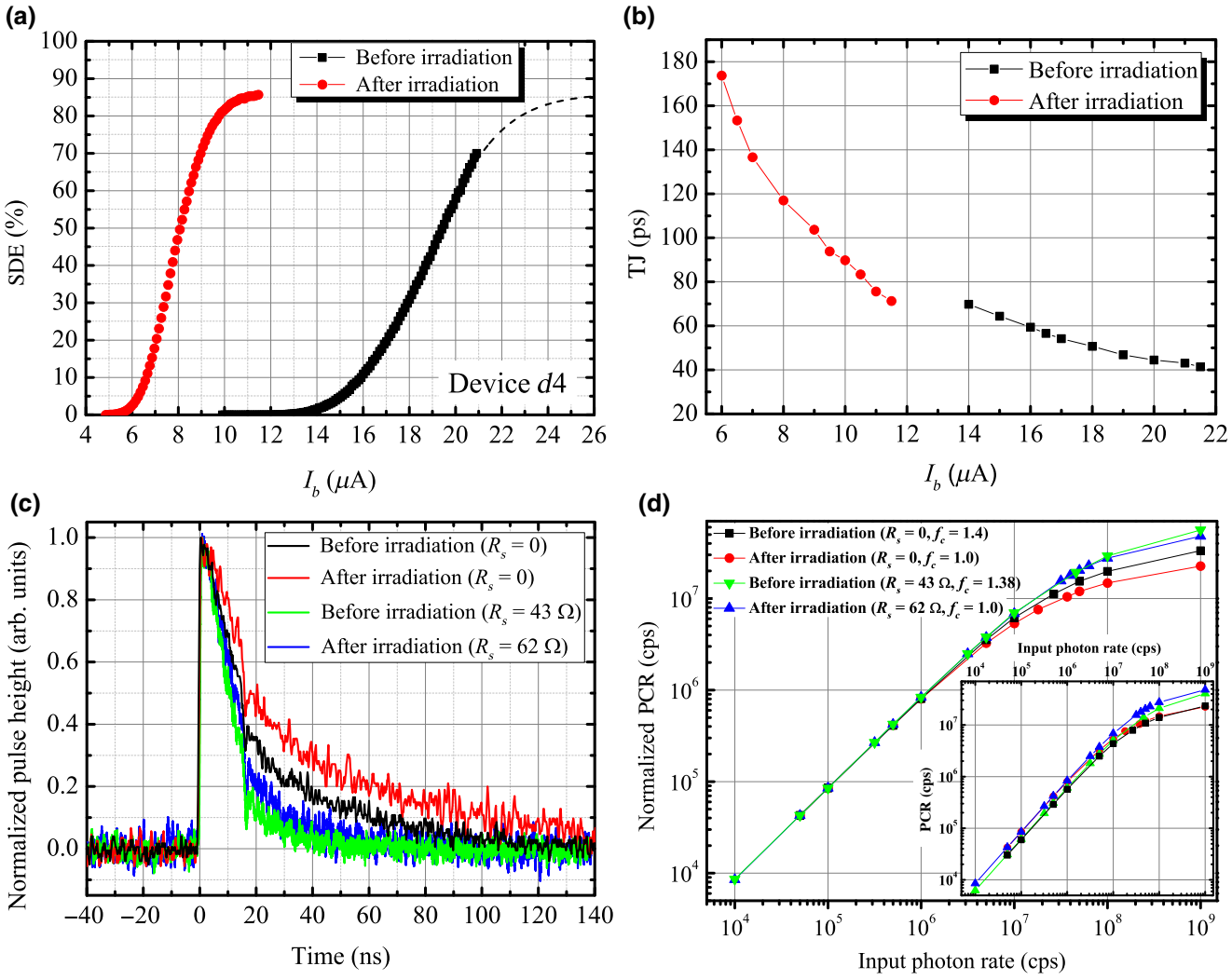

FIG. 10. Comparisons of detector performance before and after ion irradiation for the same device *d*4. (a) SDE as a function of bias current (I_b). (b) Timing jitter (TJ) vs I_b. (c) Single shot waveforms measured with different values of series resistor (R_s). (d) Normalized photon-response count rate (PCR) dependence of input photon rate, recorded for different cases. The correction factor for each case is shown in the labels. Inset, the raw data of PCR vs input photon rate. The corresponding symbols are the same as the ones shown in the main figure.

to 71.3 ± 0.6 ps at 11.5 μA after irradiation. Notably, this magnitude of 70 ps is similar to that of an unirradiated device measured at the same bias current [54]. Thus, the increased TJ of the irradiated device can be mainly attributed to the reduced SNR of the output pulse due to the irradiation-induced reduction of the switching current (I_{sw}). Recent studies showed that SNR can be improved using a cryogenic amplifier. For example, Zadeh *et al.* reported that SNSPDs with a similar I_{sw} of 12 μA may have a TJ of about 49 ps (82 ps) with (without) using a cryogenic amplifier [18].

To measure the PCR (i.e., CR-DCR) performance of the detector, a continuous wave (cw) tunable laser (Keysight 81940A) is used as the light source. The IPR is varied by tuning the attenuation of the attenuators. Previous studies [42] have shown that PCR could be proportional to $(R_l + R_s)/L_k$, where $R_l = 50\ \Omega$ is the impedance of the output coaxial cable, and L_k is the kinetic inductance of the nanowire. Generally, L_k is proportional to the normal state resistance (R_n) of the nanowire.

Since the R_n of the irradiated devices is increased after irradiation, a reduction in the maximum PCR for the irradiated device can be expected. For example, the R_n of device $d4$ is increased by about 1.3 times after irradiation. As shown in Fig. 10(c), for the case without R_s ($R_s = 0$), the pulse-decay time of the irradiated device is increased from 20 ns to 28 ns (1/e criterion). The increase ratio of the decay time is about $28/20 \approx 1.4$, close to the increased ratio of R_n. In the PCR measurements, PCR is recorded when the detector is biased at about $0.93I_{sw}$, and a 50-Ω shunt resistor at room temperature is in parallel with the SNSPD to avoid latching. Since SDE (IDE) also changed after irradiation, to compare the PCR before (after) irradiation without considering the difference in SDE, PCR is normalized by multiplying a correction factor (f_c), which is equal to the ratio of the maximum measured SDE to the current SDE. For example, as shown in Fig. 10(a), when the detector is biased at about $0.93I_{sw}$, SDE before irradiation is about 60%, but increases to about 85% after irradiation, with a ratio $f_c = 1.4$. Figure 10(d) shows the normalized PCR as a function of IPR. $f_c = 1.4$ corresponds to the case that is measured before irradiation without R_s. With different correction factors, the normalized PCRs are overlapped in the low IPR region and nearly linearly increase with IPR. In the high IPR region, due to the limitation of dead time, the detector could not respond to all the incoming photons, resulting in a nonlinear increase of PCR. Without R_s, maximum normalized PCRs of about 33 and 23 Mcps are obtained for the detector before and after irradiation, respectively, determined at an IPR of 1×10^9 photon s^{-1}. Then, the reduction factor ($33/23 \approx 1.4$) of the normalized maximum PCR after irradiation is consistent with the changes of the decay time.

To improve the PCR performance of the detector after irradiation, R_s is applied in our experiments. Figure 10(c) also shows the response pulses before and after irradiation with R_s in series (approximately 43 and 62 Ω, respectively, both measured at room temperature). The criterion for selecting the R_s value is to maximize the switching current of the device [43]. With R_s, the pulse-decay time after (before) irradiation is reduced to about 12 (11) ns, and a normalized maximum PCR of about 48 (55) Mcps is obtained. Therefore, the reduction factor is about 1.1 (approximately equal to 55/48) for the normalized maximum PCR after irradiation with R_s.

APPENDIX C: DARK COUNT RATE OF A SNSPD BEFORE AND AFTER ION IRRADIATION

We measure the intrinsic dark count rate (iDCR) as a function of the normalized bias current (I_b/I_{sw}) for the same device $d4$ before and after the ion irradiation (at a fluence of 5×10^{16} ion cm^{-2}), as shown in Fig. 11. Here, iDCR is recorded when the device is shielded in a copper package block and cooled at low temperature. iDCRs are obtained with dark counts collected for 50 s. As reported by previous papers [56,57], the dominant mechanism of iDCR may be attributed to the current-assisted unbinding of vortex-antivortex pairs. iDCR is affected by the operating temperature (T), superconducting transition temperature (T_c), as well as I_b/I_{sw}.

In Fig. 11, iDCRs before and after irradiation are both measured at about 2.13 K. To compare the difference in iDCR(I_b/I_{sw}) curves, an onset iDCR is defined, which first exceeds 0.1 cps when I_b increases. Meanwhile, the onset iDCR is associated with a bias current, defined as the onset current (I_{os}). It can be found that I_{os} after the ion irritation

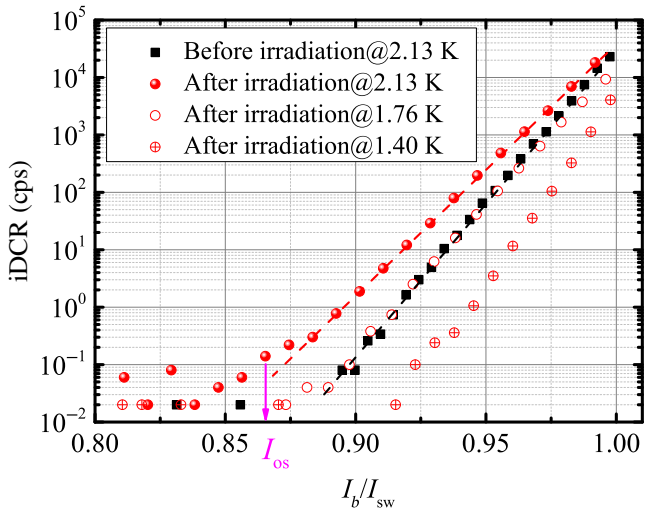

FIG. 11. Intrinsic dark count rate (iDCR) before and after irradiation as a function of the normalized bias current (I_b/I_{sw}), measured at several operating temperatures (as shown in the labels). The red and black dashed lines are drawn to guide the eye.

is reduced from $0.90I_{sw}$ to about $0.87I_{sw}$ (indicated by an arrow in Fig. 11). The onset of iDCR after irradiation shifts to a lower bias current and can be probably attributed to the ion irradiation-induced reduction of T_c. Specifically, T_c is reduced from 8.62 to 7.07 K through irradiation ($0.5R_n$ criterion for T_c). Thus, a normalized operating temperature $t_n = T/T_c$ is different in these two cases, that is, at $T = 2.13$ K, t_n is 0.25 and 0.30 before and after irradiation, respectively. To confirm this hypothesis, we remeasure iDCR vs I_b/I_{sw} by placing the irradiated device $d4$ at a 1-K cryostat (Cryomech Inc., PT407). By varying the operating temperature to about 1.76 K (corresponding to $t_n = 0.25$ for the irradiated case), the iDCR curve of the irradiated device nearly overlaps with the one of the unirradiated case. This result indicates that t_n may play a key role in the iDCR behavior. Further reducing the operating temperature to 1.40 K ($t_n = 0.20$ for the irradiated case), I_{os} shifts to about $0.92I_{sw}$.

Practically, the detector often operates in the low bias current region (generally, $\leq 0.96I_{sw}$), where iDCR can be neglected and the background DCR (bDCR) is dominant. The bDCR is proportional to the photon number of thermal radiation and/or stray light as well as IDE. Without considering the improvement in IDE, the direct influence of irradiation on DCR can be practically neglected.

APPENDIX D: IRRADIATION EFFECTS ON THE OPTICAL PARAMETERS OF THE MATERIALS

Since the thickness of the NbN thin film is much smaller than that of the SiO_2 layer, we can use a single layer of SiO_2 to simulate the effect on the top SiO_2 layer by the

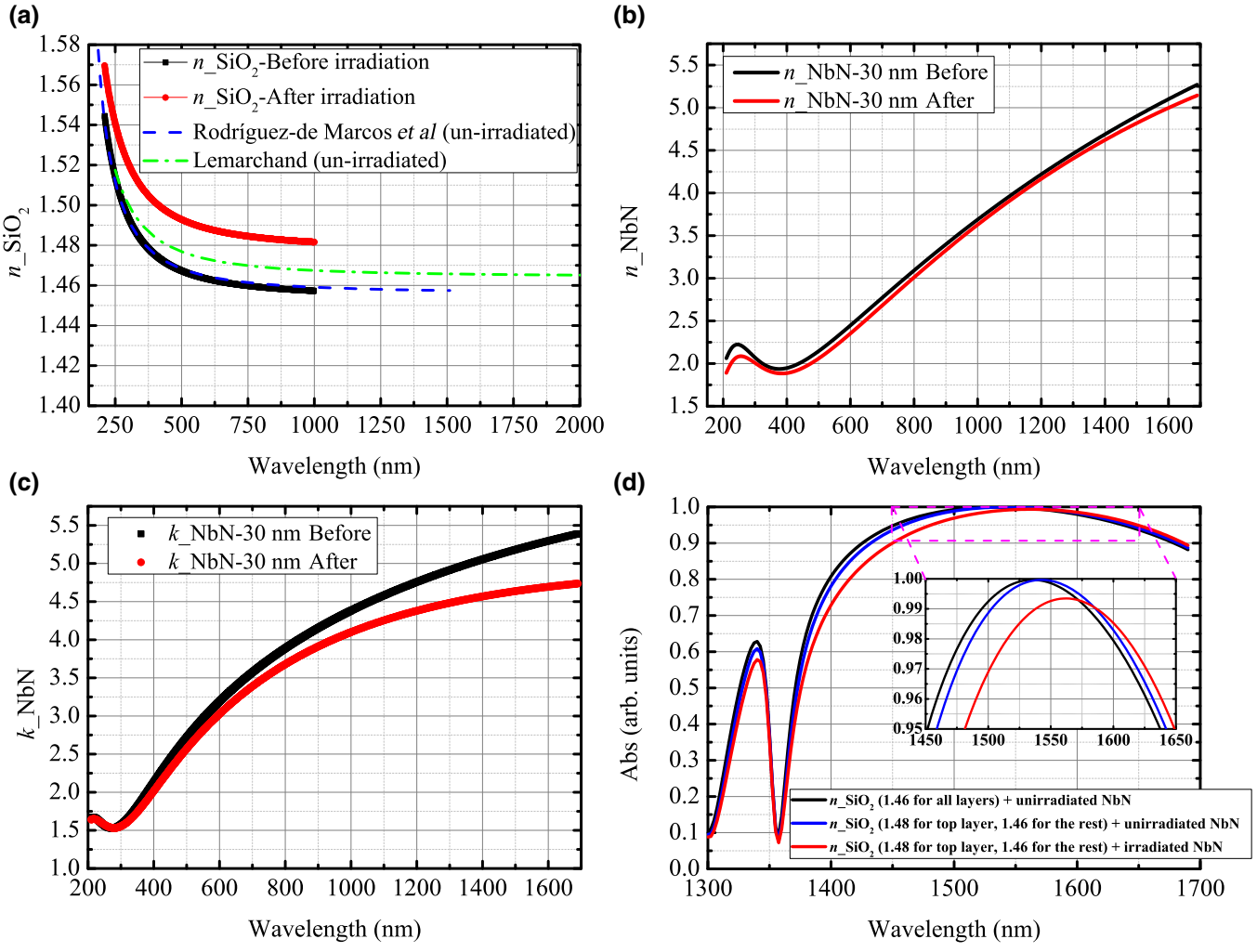

FIG. 12. (a) Refractive index of SiO_2 thin films measured before and after irradiation versus wavelength. Dashed and dashed-dotted lines are the reference data reported for unirradiated SiO_2 thin films. (b),(c) Measured refractive index (n of NbN) and extinction coefficient (k of NbN) of a 30-nm-thick NbN thin film deposited on a thermal oxidized Si wafer versus wavelength; (d) Comparison of the simulated optical absorptance (Abs) of the NbN nanowire on the DBR substrate versus wavelength by varying the n value of the top SiO_2 layer, as well as the optical parameters of the NbN thin film before and after irradiation.

He ion irradiation. Here, we measure the optical parameters (e.g., refractive index, n) of a 268-nm-thick SiO_2 layer deposited on a silicon wafer before and after irradiation, respectively, by using a commercial ellipsometer (J. A. Woollam Co. Inc., RC2). The irradiation fluence is about 5×10^{16} ion cm^{-2} at a 20-keV He ion energy.

As shown in Fig. 12(a), changes in the n value of the SiO_2 thin film induced by ion irradiation are observed, although the increment is quite small. For instance, the largest increment in the measured data appears at 283 nm, and the n value increases from 1.499 to 1.526 (an increase factor of less than 2%). Due to the high transmittance of our double-side polished wafer at near infrared (NIR), the data measured at >1000 nm are not reliable and are removed from the figure. The measured data show that He ion irradiation will result in the refractive index increasing for silica, which has been confirmed by previous papers [49,50], and could be explained by a volume compaction due to the radiation damage [58,59]. In order to predict the trend in data, two reference data of unirradiated SiO_2 thin films reported by Rodríguez-de Marcos *et al*. [60] and Lemarchand [61] are plotted in the same figure. According to the reference data, n values are nearly wavelength independent in a range of 1000–2000 nm (e.g., variation less than 0.1% for Lemarchand's data). Thus, we estimate the n value of the SiO_2 layer before and after irradiation at NIR using the measured n values at 1000 nm, which are about 1.46 and 1.48, respectively.

The optical parameters (n and extinction coefficient k) of a 30-nm-thick NbN thin film deposited on a thermal oxidized Si wafer with a 268-nm-thick SiO_2 layer are also measured before and after irradiation, as shown in Figs. 12(b) and 12(c). It can be found that the irradiation effects on the NbN thin film are reversed to the SiO_2 thin film mentioned above, that is, a reduction in n or k is found. In detail, for the NbN thin film at NIR, the reduction of n value is small (e.g., less than 2% at 1550 nm), while the reduction of the k value is relatively large and significantly wavelength dependent (approximately 11% at 1550 nm).

To reveal the changes of the optical parameters' influence on the absorptance of the NbN nanowire on a DBR substrate, we perform a numerical simulation using rigorous coupled wave analysis (RCWA) [62]. In the simulation, we use the wavelength-dependent optical parameters of NbN thin film obtained from the ellipsometer measurements before and after irradiation. Wavelength-independent (limited at NIR) n values are used for SiO_2 ($n = 1.46$) and Ta_2O_5 ($n = 2.15$) layers. In order to simulate the effects of ion irradiation, the n value of the top SiO_2 layer before and after irradiation is changed from 1.46 to 1.48. Thus, as shown in Fig. 12(d) and its inset, the irradiation effects on the top SiO_2 layer show a wavelength-shift effect (approximately 5 nm) on the optical absorptance of the NbN nanowire. The changes in the absorption of the NbN nanowire are quite small and negligible.

With the increased n values for the top SiO_2 layer, we further replace the n values of the NbN layer by the data of the irradiated NbN thin film (e.g, the n of NbN changed from $5.00 + i*5.24$ to $4.91 + i*4.67$ at 1550 nm). The peak of the simulated absorptance of the NbN nanowire shows a redshift from 1535 to 1563 nm, with a slight decrease (approximately 0.6%) in the peak value. Interestingly, the wavelength redshift effect is also observed in the reflectance measurement of the irradiated NbN thin films shown in Fig. 5 (e.g., fluence $= 0$ and 5×10^{16} ion cm^{-2}, a relative redshift of approximately 22 nm). Also, an approximately 0.2% increase in the measured minimum reflectance of the irradiated NbN thin film is found. The numerical simulation may qualitatively explain the results mentioned above. The simulation also indicates that the irradiation-induced changes of the optical parameters of NbN may lead to the changes in absorptance (reflectance). However, due to the presence of the DBR cavity, the effects caused by the changes of the optical parameters of NbN are weakened, especially at the resonant wavelength of 1550 nm. For example, in Fig. 12(d), the variations of the nanowire's absorptance near the resonant wavelengths (e.g., 1550 ± 40 nm) is less than 2%, which is smaller than our SDE measurement accuracy. Thus, we can conclude that the changes of the saturated values of SDE at 1550 nm shown in Fig. 6 are mainly caused by the enhanced intrinsic detection efficiency of nanowire, not by the irradiation-induced changes of the optical parameters.

[1] Z. Li and F. Chen, Ion beam modification of two-dimensional materials: Characterization, properties, and applications, Appl. Phys. Rev. **4**, 011103 (2017).

[2] Y. Liu, Z. Gao, Y. Tan, and F. Chen, Enhancement of out-of-plane charge transport in a vertically stacked two-dimensional heterostructure using point defects, Acs Nano **12**, 10529 (2018).

[3] X. Ou, Y. Shuai, W. B. Luo, P. F. Siles, R. Koegler, J. Fiedler, H. Reuther, S. Q. Zhou, R. Huebner, S. Facsko, M. Helm, T. Mikolajick, O. G. Schmidt, and H. Schmidt, Forming-free resistive switching in multiferroic $BiFeO_3$ thin films with enhanced nanoscale shunts, Acs Appl. Mater. Inter. **5**, 12764 (2013).

[4] Q. Jia, J. Grenzer, H. B. He, W. Anwand, Y. D. Ji, Y. Yuan, K. Huang, T. G. You, W. J. Yu, W. Ren, X. Z. Chen, M. K. Liu, S. Facsko, X. Wang, and X. Ou, 3D local manipulation of the metal-insulator transition behavior in VO_2 thin film by defect-induced lattice engineering, Adv. Mater. Interfaces **5**, 1701268 (2018).

[5] N. Kobayashi, G. Linker, and O. Meyer, Structural disorder and superconducting transition temperature of ion-irradiated NbC, J. Phys. F: Met. Phys. **17**, 1491 (1987).

[6] J. Y. Juang, D. A. Rudman, J. Talvacchio, and R. B. van Dover, Effects of ion irradiation on the normal state and superconducting properties of NbN thin films, Phys. Rev. B **38**, 2354 (1988).

[7] S. A. Cybart, E. Y. Cho, T. J. Wong, B. H. Wehlin, M. K. Ma, C. Huynh, and R. C. Dynes, Nano Josephson superconducting tunnel junctions in $YBa_2Cu_3O_{7-\delta}$ directly patterned with a focused helium ion beam, Nat. Nanotechnol. **10**, 598 (2015).

[8] M. Leroux, K. J. Kihlstrom, S. Holleis, M. W. Rupich, S. Sathyamurthy, S. Fleshler, H. P. Sheng, D. J. Miller, S. Eley, L. Civale, A. Kayani, P. M. Niraula, U. Welp, and W.-K. Kwok, Rapid doubling of the critical current of $YBa_2Cu_3O_{7-\delta}$ coated conductors for viable high-speed industrial processing, Appl. Phys. Lett. **107**, 192601 (2015).

[9] L. Civale, A. D. Marwick, T. K. Worthington, M. A. Kirk, J. R. Thompson, L. Krusin-Elbaum, Y. Sun, J. R. Clem, and F. Holtzberg, Vortex Confinement by Columnar Defects in $YBa_2Cu_3O_7$ Crystals: Enhanced Pinning at High Fields and Temperatures, Phys. Rev. Lett. **67**, 648 (1991).

[10] A. Boltasseva and H. A. Atwater, Low-loss plasmonic metamaterials, Science **331**, 290 (2011).

[11] G. N. Gol'tsman, O. Okunev, G. Chulkova, A. Lipatov, A. Semenov, K. Smirnov, B. Voronov, A. Dzardanov, C. Williams, and R. Sobolewski, Picosecond superconducting single-photon optical detector, Appl. Phys. Lett. **79**, 705 (2001).

[12] P. Gregshammer, H. W. Weber, R. T. Kampwirth, and K. E. Gray, The effects of high-fluence neutron irradiation on the superconducting properties of magnetron sputtered NbN films, J. Appl. Phys. **64**, 1301 (1988).

[13] F. Marsili, V. B. Verma, J. A. Stern, S. Harrington, A. E. Lita, T. Gerrits, I. Vayshenker, B. Baek, M. D. Shaw, R. P. Mirin, and S. W. Nam, Detecting single infrared photons with 93% system efficiency, Nat. Photon. **7**, 210 (2013).

[14] W. J. Zhang, L. X. You, H. Li, J. Huang, C. L. Lv, L. Zhang, X. Y. Liu, J. J. Wu, Z. Wang, and X. M. Xie, NbN superconducting nanowire single photon detector with efficiency over 90% at 1550 nm wavelength operational at compact cryocooler temperature, Sci. China Phys. Mech. Astron. **60**, 120314 (2017).

[15] W. J. Zhang, X. Y. Yang, H. Li, L. X. You, C. L. Lv, L. Zhang, C. J. Zhang, X. Y. Liu, Z. Wang, and X. M. Xie, Fiber-coupled superconducting nanowire single-photon detectors integrated with a bandpass filter on the fiber end-face, Supercond. Sci. Technol. **31**, 035012 (2018).

[16] W. J. Zhang, J. Huang, C. J. Zhang, L. X. You, C. L. Lv, L. Zhang, H. Li, Z. Wang, and X. M. Xie, A 16-pixel interleaved superconducting nanowire single-photon detector array with a maximum count rate exceeding 1.5 GHz, IEEE Trans. Appl. Supercond. **29**, 1 (2019).

[17] J. J. Wu, L. X. You, S. J. Chen, H. Li, Y. H. He, C. L. Lv, Z. Wang, and X. M. Xie, Improving the timing jitter of a superconducting nanowire single-photon detection system, Appl. Opt. **56**, 2195 (2017).

[18] I. E. Zadeh, J. W. N. Los, R. B. M. Gourgues, V. Steinmetz, G. Bulgarini, S. M. Dobrovolskiy, V. Zwiller, and S. N. Dorenbos, Single-photon detectors combining high efficiency, high detection rates, and ultra-high timing resolution, APL Photon. **2**, 111301 (2017).

[19] Q.-C. Sun, Y.-L. Mao, S.-J. Chen, W. Zhang, Y.-F. Jiang, Y.-B. Zhang, W.-J. Zhang, S. Miki, T. Yamashita, H. Terai, X. Jiang, T.-Y. Chen, L.-X. You, X.-F. Chen, Z. Wang, J.-Y. Fan, Q. Zhang, and J.-W. Pan, Quantum teleportation with independent sources and prior entanglement distribution over a network, Nat. Photon. **10**, 671 (2016).

[20] M. E. Grein, A. J. Kerman, E. A. Dauler, M. M. Willis, B. Romkey, R. J. Molnar, B. S. Robinson, D. V. Murphy, and D. M. Boroson, An optical receiver for the Lunar Laser Communication Demonstration based on photon-counting superconducting nanowires, SPIE Sens. Technol. + Appl. **9492**, 949208 (2015).

[21] A. McCarthy, N. J. Krichel, N. R. Gemmell, X. Ren, M. G. Tanner, S. N. Dorenbos, V. Zwiller, R. H. Hadfield, and G. S. Buller, Kilometer-range, high resolution depth imaging via 1560 nm wavelength single-photon detection, Opt. Express **21**, 8904 (2013).

[22] H. Zhou, Y. He, L. You, S. Chen, W. Zhang, J. Wu, Z. Wang, and X. Xie, Few-photon imaging at 1550 nm using a low-timing-jitter superconducting nanowire single-photon detector, Opt. Express **23**, 14603 (2015).

[23] Y. Liu, Q. Zhao, M.-H. Li, J.-Y. Guan, Y. Zhang, B. Bai, W. Zhang, W.-Z. Liu, C. Wu, X. Yuan, H. Li, W. J. Munro, Z. Wang, L. You, J. Zhang, X. Ma, J. Fan, Q. Zhang, and J.-W. Pan, Device-independent quantum random-number generation, Nature **562**, 548 (2018).

[24] L. K. Shalm, *et al.*, Strong Loophole-Free Test of Local Realism, Phys. Rev. Lett. **115**, 250402 (2015).

[25] L. Chen, D. Schwarzer, V. B. Verma, M. J. Stevens, F. Marsili, R. P. Mirin, S. W. Nam, and A. M. Wodtke, Mid-infrared laser-induced fluorescence with nanosecond time resolution using a superconducting nanowire single-photon detector: New technology for molecular science, Accounts Chem. Res. **50**, 1400 (2017).

[26] M. R. Bolcar *et al.*, The Large UV/Optical/Infrared Surveyor (LUVOIR): Decadal Mission concept design update, SPIE Opt. Eng. + Appl. **10398**, 1039809 (2017).

[27] A. Semenov, A. Engel, H. W. Hubers, K. Il'in, and M. Siegel, Spectral cut-off in the efficiency of the resistive state formation caused by absorption of a single-photon in current-carrying superconducting nano-strips, Eur. Phys. J. B **47**, 495 (2005).

[28] J. J. Renema, R. Gaudio, Q. Wang, Z. Zhou, A. Gaggero, F. Mattioli, R. Leoni, D. Sahin, M. J. A. de Dood, A. Fiore, and M. P. van Exter, Experimental Test of Theories of the Detection Mechanism in a Nanowire Superconducting Single Photon Detector, Phys. Rev. Lett. **112**, 117604 (2014).

[29] A. Engel, J. J. Renema, K. Il'in, and A. Semenov, Detection mechanism of superconducting nanowire single-photon detectors, Supercond. Sci. Technol. **28**, 114003 (2015).

[30] Y. Korneeva, I. Florya, S. Vdovichev, M. Moshkova, N. Simonov, N. Kaurova, A. Korneev, and G. Goltsman, Comparison of hot spot formation in NbN and MoN thin superconducting films after photon absorption, IEEE Trans. Appl. Supercond. **27**, 1 (2017).

[31] T. Yamashita, S. Miki, H. Terai, and Z. Wang, Low-filling-factor superconducting single photon detector with high system detection efficiency, Opt. Express **21**, 27177 (2013).

[32] S. Konstantin, D. Alexander, V. Yury, M. Pavel, Z. Philipp, A. Andrey, and S. Vitaliy, NbN single-photon detectors with saturated dependence of quantum efficiency, Supercond. Sci. Technol. **31**, 035011 (2018).

[33] F. Marsili, F. Bellei, F. Najafi, A. E. Dane, E. A. Dauler, R. J. Molnar, and K. K. Berggren, Efficient single photon

detection from 500 nm to 5 mum wavelength, Nano Lett. **12**, 4799 (2012).

[34] M. Caloz, M. Perrenoud, C. Autebert, B. Korzh, M. Weiss, C. Schönenberger, R. J. Warburton, H. Zbinden, and F. Bussières, High-detection efficiency and low-timing jitter with amorphous superconducting nanowire single-photon detectors, Appl. Phys. Lett. **112**, 061103 (2018).

[35] A. Engel, A. Aeschbacher, K. Inderbitzin, A. Schilling, K. Il'in, M. Hofherr, M. Siegel, A. Semenov, and H.-W. Hübers, Tantalum nitride superconducting single-photon detectors with low cut-off energy, Appl. Phys. Lett. **100**, 062601 (2012).

[36] X. Zhang, A. Engel, Q. Wang, A. Schilling, A. Semenov, M. Sidorova, H. W. Hübers, I. Charaev, K. Ilin, and M. Siegel, Characteristics of superconducting tungsten silicide WSi_{1-x} for single photon detection, Phys. Rev. B **94**, 174509 (2016).

[37] F. Marsili, M. J. Stevens, A. Kozorezov, V. B. Verma, C. Lambert, J. A. Stern, R. D. Horansky, S. Dyer, S. Duff, D. P. Pappas, A. E. Lita, M. D. Shaw, R. P. Mirin, and S. W. Nam, Hotspot relaxation dynamics in a current-carrying superconductor, Phys. Rev. B **93**, 094518 (2016).

[38] Y. Ivry, J. J. Surick, M. Barzilay, C.-S. Kim, F. Najafi, E. Kalfon-Cohen, A. D. Dane, and K. K. Berggren, Superconductor–superconductor bilayers for enhancing single-photon detection, Nanotechnology **28**, 435205 (2017).

[39] M. G. Tanner, C. M. Natarajan, V. K. Pottapenjara, J. A. O'Connor, R. J. Warburton, R. H. Hadfield, B. Baek, S. W. Nam, S. N. Dorenbos, and E. B. Urena, Enhanced telecom wavelength single-photon detection with NbTiN superconducting nanowires on oxidized silicon, Appl. Phys. Lett. **96**, 221109 (2010).

[40] A. E. Dane, A. N. McCaughan, D. Zhu, Q. Zhao, C.-S. Kim, N. Calandri, A. Agarwal, F. Bellei, and K. K. Berggren, Bias sputtered NbN and superconducting nanowire devices, Appl. Phys. Lett. **111**, 122601 (2017).

[41] J. F. Ziegler, M. D. Ziegler, and J. P. Biersack, SRIM–The stopping and range of ions in matter (2010), Nucl. Instrum. Methods Phys. Res., Sect. B **268**, 1818 (2010).

[42] J. K. W. Yang, A. J. Kerman, E. A. Dauler, V. Anant, M. R. Kristine, and K. K. Berggren, Modeling the electrical and thermal response of superconducting nanowire single-photon detectors, IEEE Trans. on Appl. Supercond. **17**, 5 (2007).

[43] C. J. Zhang, W. J. Zhang, J. Huang, L. X. You, H. Li, C. L. lv, T. Sugihara, M. Watanabe, H. Zhou, Z. Wang, and X. M. Xie, NbN superconducting nanowire single-photon detector with an active area of 300 μm-in-diameter, AIP Adv. **9**, 075214 (2019).

[44] J. Bardeen, L. N. Cooper, and J. R. Schrieffer, Theory of superconductivity, Phys. Rev. **108**, 1175 (1957).

[45] M. Tinkham, *Introduction to superconductivity* (Courier Dover Publications, New York, 2012).

[46] N. R. Werthamer, E. Helfand, and P. C. Hohenberg, Temperature and purity dependence of the superconducting critical field, H_{c2}. III. Electron spin and spin-orbit effects, Phys. Rev. **147**, 295 (1966).

[47] Z. Wang, A. Kawakami, Y. Uzawa, and B. Komiyama, Superconducting properties and crystal structures of single-crystal niobium nitride thin films deposited at ambient substrate temperature, J. Appl. Phys. **79**, 7837 (1996).

[48] R. Romestain, B. Delaet, P. Renaud-Goud, I. Wang, C. Jorel, J. C. Villegier, and J. P. Poizat, Fabrication of a superconducting niobium nitride hot electron bolometer for single-photon counting, New J. Phys. **6**, 129 (2004).

[49] R. L. Hines and R. Arndt, Radiation effects of bombardment of quartz and vitreous silica by 7.5-kev to 59-kev positive ions, Phys. Rev. **119**, 623 (1960).

[50] G. W. Arnold, Ion implantation effects in glasses, Radiat. Eff. **65**, 17 (1982).

[51] L. X. You, J. Quan, Y. Wang, Y. X. Ma, X. Y. Yang, Y. J. Liu, H. Li, J. G. Li, J. Wang, J. T. Liang, Z. Wang, and X. M. Xie, Superconducting nanowire single photon detection system for space applications, Opt. Express **26**, 2965 (2018).

[52] A. Engel, J. Lonsky, X. Zhang, and A. Schilling, Detection mechanism in SNSPD: Numerical results of a conceptually simple, yet powerful detection model, IEEE Trans. Appl. Supercond. **25**, 1 (2015).

[53] H. Wang, W. Li, X. Jiang, Y. M. He, Y. H. Li, X. Ding, M. C. Chen, J. Qin, C. Z. Peng, C. Schneider, M. Kamp, W. J. Zhang, H. Li, L. X. You, Z. Wang, J. P. Dowling, S. Höfling, C.-Y. Lu, and J.-W. Pan, Toward Scalable Boson Sampling with Photon Loss, Phys. Rev. Lett. **120**, 230502 (2018).

[54] L. X. You, X. Y. Yang, Y. H. He, W. X. Zhang, D. K. Liu, W. J. Zhang, L. Zhang, L. Zhang, X. Y. Liu, S. J. Chen, Z. Wang, and X. M. Xie, Jitter analysis of a superconducting nanowire single photon detector, AIP Adv. **3**, 072135 (2013).

[55] M. Ejrnaes, A. Casaburi, O. Quaranta, S. Marchetti, A. Gaggero, F. Mattioli, R. Leoni, S. Pagano, and R. Cristiano, Characterization of parallel superconducting nanowire single photon detectors, Supercond. Sci. Technol. **22**, 055006 (2009).

[56] H. Bartolf, A. Engel, A. Schilling, K. Il'in, M. Siegel, H. W. Hübers, and A. Semenov, Current-assisted thermally activated flux liberation in ultrathin nanopatterned NbN superconducting meander structures, Phys. Rev. B **81**, 024502 (2010).

[57] T. Yamashita, S. Miki, K. Makise, W. Qiu, H. Terai, M. Fujiwara, M. Sasaki, and Z. Wang, Origin of intrinsic dark count in superconducting nanowire single-photon detectors, Appl. Phys. Lett. **99**, 161105 (2011).

[58] E. P. EerNisse, Compaction of ion-implanted fused silica, J. Appl. Phys. **45**, 167 (1974).

[59] A. P. Webb and P. D. Townsend, Refractive index profiles induced by ion implantation into silica, J. Phys. D: Appl. Phys. **9**, 1343 (1976).

[60] L. V. Rodríguez-de Marcos, J. I. Larruquert, J. A. Méndez, and J. A. Aznárez, Self-consistent optical constants of SiO_2 and Ta_2O_5 films, Opt. Mater. Express **6**, 3622 (2016).

[61] F. Lemarchand, unpublished. available from: https://refractiveindex.info.

[62] L. Zhang, RicWaA-Rigorous Coupled Wave Analysis (RCWA) (2010). Available from: http://www-personal.umich.edu/∼zlei/.